EXPERIMENTAL AND NUMERICAL STUDY ON A STRAIGHT EXHAUST PIPE

S.-M. Liang [*]

Department of Computer Application Engineering
Far East University
Tainan, Taiwan 74448, R.O.C.

C.-J. Wang [**]

Department of Mechanical Engineering
Far East University
Tainan, Taiwan 74448, R.O.C.

ABSTRACT

In this study, radiated noise is investigated by experimental and numerical methods for a straight exhaust pipe of diameter 23mm that replaces the original exhaust pipe of a motorcycle of EZ 125cc provided by Kwang Yang Motor Co. In experiment, temperature, pressure and flow speed of the exhausted gas have been measured for different engine speeds ranging from 3000-5000rpm without loading. Sound pressure levels (*SPL*) at a distance of 0.5m from the exhaust pipe exit for different inclination angles (0° ~ 90°) were recorded and compared with the result of simulation. In numerical simulation, a high-resolution 5th-order Euler solver was used and conducted on a parallel computation system with a cluster of 4 personal computers with dual processors. It is found that the back-and-forth reflection of expansion waves inside the pipe due to the shock wave diffraction around the pipe exit is the mechanism of radiating sound waves from the exhaust pipe. The numerical result shows the exhausted-gas flow with complicated vortex rings and its associated acoustic field. The acoustic field indicates that there are three sound lobes with different directivities for the engine speed of 4000rpm.

Keywords: Blast wave, Vortex ring, Euler equations, Sound pressure level, Radiated noise.

1. INTRODUCTION

Motorcycles are still an important traffic tool in Taiwan. The problem associated with motorcycles is the exhausted gases and noise generated from exhaust pipes. This paper concerns only with the noise problem. The standard of noise control [1] requires 90dBA and 75dBA in cases of stationary and accelerated noise for motorcycles of engine volume 50cc ~ 100cc, respectively. Further reducing motorcycle's noise is desirable. An exhaust pipe usually has an expansion chamber with a catalytic converter, causing a very complicated flow to be analyzed. Due to the complicity of a real exhaust pipe of a motorcycle, a simplified, straight, circular exhaust pipe of 59cm in length and 23mm in diameter without a catalyst converter and an expansion chamber pipe is considered for the present study. In order to investigate the flow and acoustic fields associated with the exhaust pipe, we use both experimental and numerical simulation techniques. Both experimental and numerical results obtained will pave a stepping stone for studying the problem of noise reduction.

Noise associated with an exhaust pipe of automotive internal engines can be classified into three kinds: Turbulence noise, vibration noise and radiated noise. In this study, only radiated noise is considered. Since the exhaust gas emitted from an internal engine is a pulsating flow with blast waves, the sound sources of radiated noise mainly involved of shock wave, vortex ring and their interaction. A blast wave is a so-called reverse "N" wave in a pressure profile which has a structure of two shock waves and expansion waves. Although linear acoustic theory [2] has been developed and widely used, but it fails in the present study because of the existing shock waves. The mechanism of radiated noise generation from the exhaust pipe is still unclear. Because the calculation of acoustic field needs a tremendously large time on a single computer, we use parallel computational flow dynamics (CFD) to study the mechanism of radiation noise generation through the predicted flow and acoustic fields.

In the past, there were many papers reported about the noise generated from an exhaust pipe. Due to the paper space, only some recent papers are mentioned here. Kim and Setoguchi [3] investigated the downstream pressure variation of a shocked flow discharged from an open ended shock-tube with a circular baffle plate at the tube exit by using both experimental and numerical methods. Higashiyama and Iwamoto [4] experimentally studied the noise generated by a pulsating flow downstream of a pipe end. Their data also showed the directivity of sound pressure. Endo *et al.* [5] analyzed the noise relation between the directional angle and the rotation speed of a rotary valve in detail.

[*] Professor, corresponding author [**] Graduate student

DOI : 10.1017/jmech.2011.62
Copyright © 2011 The Society of Theoretical and Applied Mechanics, R.O.C.
https://doi.org/10.1017/jmech.2011.62 Published online by Cambridge University Press

They also compared the sound pressure distributions for different directional angles at various rotation speeds of the rotary valve. Chen and Liang [6] investigated a planar blast/vortex interaction and its generated noise, and found four sounds generated for the blast/vortex interaction in a form of interlacing compression and expansion. Their result was well contrasted to that for the corresponding shock/vortex interaction studied by Inoue and Hattori [7]. Liang and Lo [8] numerically investigated shock/vortex interactions induced by blast wave diffraction around a 90° sharp convex corner, and found that a pair of vortices could be generated by the diffracted blast wave. Later, Liang *et al*. [9] numerically investigated the detailed spiral flow structure, induced by a planar shock wave, near a two-dimensional circular duct exit. They also showed some computational holographic interferograms near the duct exit for different incident shock Mach numbers. Kim *et al*. [10] studied weak shock propagations through an exhaust silencer system for incident shock Mach numbers of 1.01 and 1.30, and designed several silencers and compared decayed histories of shock waves.

For the very recent works, Gabard and Astley [11] presented an analytical model for sound radiation from a semi-infinite unflanged annular duct and far-field directivity of sound radiation. Gabard [12] reported a theoretical study of the sound radiation through jet exhausts. His study was focused on the transition from the near-field to far-field acoustics. Demir and Rienstra [13] showed the sound waves issuing from the exit of an annular duct with a lined centerbody. In these studies, the flow has no shock waves involved and the linear acoustic theory can be applied. For the exhaust flow with shock waves, the linear acoustic theory fails to be applied. The acoustic problem of an exhaust flow has great challenge for parallel CFD by using the Navier-Stokes equations with a laminar or turbulence model. In order to capture both the blast and sound waves involved in the exhaust flow, a high-resolution is needed and the inviscid exhaust flow is assumed for practical numerical simulation.

2. EXPERIMENTAL AND NUMERICAL APPROACHES

2.1 Experimental Method

2.1.1 Experimental Setup

In experiment, a motorcycle of EZ 125cc, provided by Kwang Yang Motor Co., with the aforementioned straight circular pipe was used, as shown in Fig. 1. The corresponding simulation region is enclosed by a square. The circular pipe was supported by an extra holder that was fixed on the motorcycle in order to avoid its vibration during engine operation. Moreover, an electronic revolution counter (Kitaco Co.) was additionally built on it. The engine speed was set to range from 3000rpm to 5000rpm with an increment of 1000rpm. There are three holes of diameter 2mm, denoted by holes A, B and C respectively, near the pipe exit for measuring the static pressure and temperature, referring to Fig. 1. The distances from holes A, B and C to the pipe exit are 46.46mm, 46.92mm and 47.39mm respectively. These data of the static pressures and temperatures at these three points will be used for numerical simulation. The purpose of the measured data at these three holes is to satisfy the need of a 5th-order accuracy scheme used in numerical simulation.

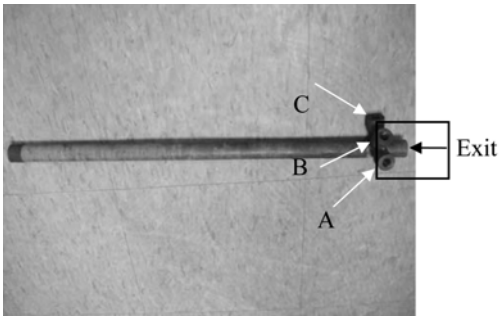


Fig. 1 A straight circular exhaust pipe

2.1.2 Pressure Measurement

For pressure measurement, we simultaneously used three pressure sensors of type 111A21 (PCB Piezotronics Inc.). The pressure sensor was connected with a constant-current power/signal conditioner of type 482A05 and subsequently with an oscilloscope of type DSO5014A (Agilent Technologies Co.). The pressure sensor was built inside a water-cooled adaptor (PCB-064B02) for protecting high-temperature damage. The setup of pressure measurement is schematically shown in Fig. 2. Notice that a bullet-typed sheath was built in the hole to accommodate the water-cooled adaptor.

2.1.3 Temperature Measurement

For temperature measurement, a K-type thermal couple was used and connected to a data acquisition and a control system of type ADAM-5000 (Advantech Co.). The system transferred the measured temperature data to a personal computer through a RS-232 cable. The thermal couple can measure a temperature of 40-1200°C. In this study, the maximum error is about ±2.5°C for the temperature range of 40-333°C.

2.1.4 Measurement of Average Flow Speed

A pitot tube with a guide tube was used for measuring the average flow speed in the tailpipe. The guide tube has two open ends. One end was placed at the exit of the pipe; the other end was connected to the pitot tube. The average flow speed is calculated based on the Bernoulli equation.

2.1.5 Measurement of Sound Pressure Level

For sound pressure level (*SPL*) measurement, an anechoic room provided by Automotive Research & Testing Center, located at Chang-Hua, Taiwan, was employed. The *SPL* was measured by a microphone of B & K-4190 (Brüel & Kjær Inc.) located at a distance of 0.25m and of 0.5m from the pipe exit for different inclination angles (15° ~ 90°) with respective to the pipe centerline. The microphone was connected with a

https://doi.org/10.1017/jmech.2011.62 Published online by Cambridge University Press

multi-channel data acquisition system of B & K-3550. Notice that the microphone height should be the same as that of the pipe exit. A large circular pipe located far downstream of the pipe exit was used to suction out the exhausted gas, as shown in Fig. 2.

2.2 Numerical Simulation

2.2.1 Governing Equations

With the neglect of heat transfer effects and flow viscosity in the exhaust gas flow, the governing equations are the Euler equations that represent the conservations of mass, momentum and energy. The Euler equations can be written in a conservative form after normalization as below.

$$\frac{\partial Q}{\partial t}+\frac{\partial F}{\partial z}+\frac{\partial G}{\partial r}+H=0 \tag{1}$$

$$Q=\begin{bmatrix}\rho\\ \rho V_z\\ \rho V_r\\ e\end{bmatrix},\ F=\begin{bmatrix}\rho V_z\\ \rho V_z^2+p\\ \rho V_z V_r\\ V_z(e+p)\end{bmatrix},$$

$$G=\begin{bmatrix}\rho V_r\\ \rho V_z V_r\\ \rho V_r^2+p\\ V_r(e+p)\end{bmatrix},\ H=\frac{1}{r}\begin{bmatrix}\rho V_r\\ \rho V_z V_r\\ \rho V_r^2\\ V_r(e+p)\end{bmatrix}$$

Here vector Q denotes a conservative variable, ρ the density, (V_z, V_r) the flow velocity components in the streamwise direction z and radial direction r, respectively, and e the total energy per unit volume. (F, G) are the flux vector components in the (z, r) direction respectively, and H the source term due to the axis symmetry. Assume the exhausted gas is a perfect gas. We have the equation of state that relates the pressure, density, total energy and velocity:

$$p=(\gamma-1)\left[e-\frac{1}{2}\rho(V_z^2+V_r^2)\right] \tag{2}$$

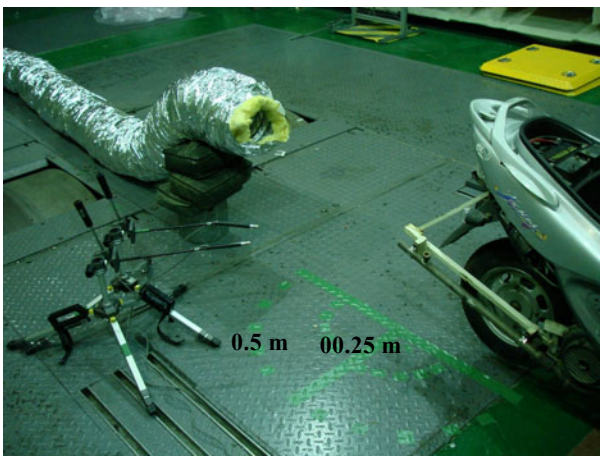


Fig. 2 Setup of sound pressure level measurement

where γ is the ratio of specific heats. It was assumed to be $\gamma = 1.4$ for a perfect gas and 1.3 for an exhaust gas. Notice that the flow variables in Eq. (1) have been normalized by

$$\rho=\frac{\tilde{\rho}}{\tilde{\rho}_{ref}},\ V_z=\frac{\tilde{V}_z}{\tilde{c}_{ref}},\ V_r=\frac{\tilde{V}_r}{\tilde{c}_{ref}},\ e=\frac{\tilde{e}}{\tilde{\rho}_{ref}\tilde{c}_{ref}^2},$$
$$z=\frac{\tilde{z}}{\tilde{l}_{ref}},\ r=\frac{\tilde{r}}{\tilde{l}_{ref}},\ t=\frac{\tilde{t}}{\tilde{l}_{ref}/\tilde{c}_{ref}},\ p=\frac{\tilde{p}}{\tilde{\rho}_{ref}\tilde{c}_{ref}^2} \tag{3}$$

where the subscript "*ref*" denotes a reference condition, the superscript "~" the dimensional quantities, $\tilde{c}_{ref}$ the sound speed chosen to be at a room temperature of 15°C, and $\tilde{l}_{ref}$ the characteristic length chosen to be the pipe diameter ($\tilde{D}$ = 23mm). Note that, in order to capture the shock and sound waves, the dimensionless time is scaled up by about an order of magnitude of 1.5×10^4 from the physical time, resulting in a large computational time for a single computer. To overcome this difficulty, parallel computation with 4 personal computers with dual processors were set up. For this, the Euler solver with a function of parallel computation was developed, which is described below.

2.2.2 Numerical Scheme

To numerically solve Eq. (1), we used a fourth-order non-TVD Runge-Kutta method for time integration, and a fifth-order weighted essentially non-oscillation (WENO) scheme [14] for spatial discretization of convective terms. The Courant number was chosen to be 0.4. The 5th-order WENO scheme is constructed in a finite volume fashion for ensuring the mass, momentum and energy conservations in each finite volume.

2.2.3 Initial and Boundary Conditions

The computational domain was chosen to be $\{(z, r)|-2 \le z \le 6,\ 0 \le r \le 6.5\}$, as shown in Fig. 3(a). Note that the coordinate origin was set at the center of the pipe exit.

The initial condition is a quiescent flow inside and downstream the pipe at a standard atmospheric condition. At the pipe inlet ($z = -2$), the dynamic pressure, average flow velocity and average temperature measured from experiments for an engine speed were prescribed. The dynamic pressure is a periodic behavior during an engine cycle, resulting in an unsteady flow with sound waves discharged from the pipe.

The slip condition is imposed on the pipe wall. On the centerline, a symmetry condition is assumed in order to save computational time and computer memory for the axi-symmetric flow. The flow variables at the dummy cells for the symmetry condition are given by

$$\begin{bmatrix}\rho\\ V_z\\ V_r\\ e\end{bmatrix}_{dum+i}=\begin{bmatrix}\rho\\ V_z\\ -V_r\\ e\end{bmatrix}_{dum-1-i},\quad i=0,1,2 \tag{4}$$

https://doi.org/10.1017/jmech.2011.62 Published online by Cambridge University Press

The non-reflecting boundary condition of Thompson [15] is specified at the left ($z = -2$), lower ($r = 6.5$) and right ($z = 6$) boundaries. For example, along the $r = 6.5$ boundary, we have

$$\frac{\partial Q}{\partial t}+\frac{\partial F}{\partial z}+\frac{1}{J}M\left(L^{-1}\Lambda_r L\frac{\partial U}{\partial r}\right)=0 \tag{5}$$

where $M \equiv \partial Q/\partial U$ is the Jacobian matrix, $U = [\rho\ V_z\ V_r\ e\ ]^T$ the primitive variables, and J the Jacobian (the volume of a control volume), and L the left eigenvector of the Jacobian matrix, $\partial Q/\partial U$. For outgoing waves with the positive eigenvalues, we can obtain flow properties by interpolation at the outer boundary. For incoming waves with the negative eigenvalues, the corresponding term will be replaced by zero. In the same way, we can treat other boundaries.

2.3 Parallel Computation

A cluster system of 4 personal computers was set up. The hardware includes Central Processing Units (CPUs), network cards, routers, and Random Access Memories (RAMs). The specification of CPU is of type AMD64-4600 (Advanced Micro Devices, Inc.). The specification of network card is 1Gbps (bits per second), 1Gbps for router, and 1Gbyte for RAM. The software of operating system used is Linux Fedora 6 with a parallel-computing interface program of LAM/MPI and a programming language of Intel FORTRAN 9.

The computational domain is divided into 4 blocks (sub-domains), as shown in Fig. 3(b). In each block one computer is assigned for computation. Since the 5th-order WENO scheme is used, one to three auxiliary grid point (s) inside the indicated grey region along each common boundary, (for example, the common boundary for blocks 3 and 4,) may be used during computation inside each block. An iterative procedure is preceded, and it is terminated until a periodic solution is obtained.

2.4 Calculation of Sound Pressure Level

The sound pressure level (SPL) is defined to be

$$SPL\ (\mathrm{dB}) = 10\times\log\left(\frac{\tilde{p}_{rms}}{2\times10^{-5}\ \mathrm{Pa}}\right)^2,$$
$$\tilde{p}_{rms}=\sqrt{\sum_{i=1}^{N}\frac{(\tilde{p}_i')^2}{N-1}},\quad \tilde{p}_i'=\tilde{p}_i-\tilde{p}_{ref}\ , \tag{6}$$

at each grid point, where N is the total number of samples used. The reference pressure $\tilde{p}_{ref}$ is defined as

$$\tilde{p}_{ref}(x,y)=\frac{1}{T}\int_0^T \tilde{p}(x,y,t)\,dt \tag{7}$$

Here T for the period in a chosen residual cycle.

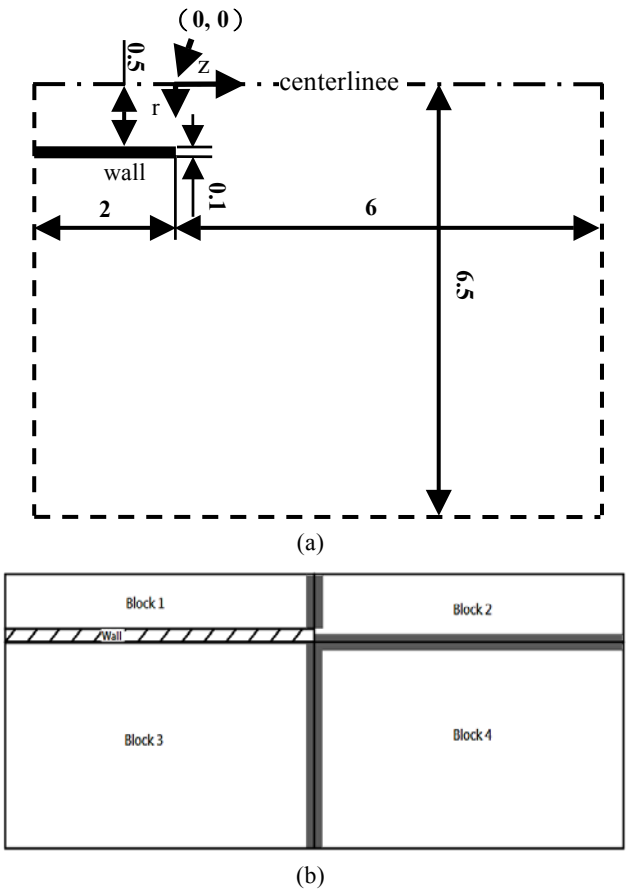


Fig. 3 (a) a computational domain and (b) its four partitioned blocks

3. RESULTS AND DISCUSSION

3.1 Measured Results

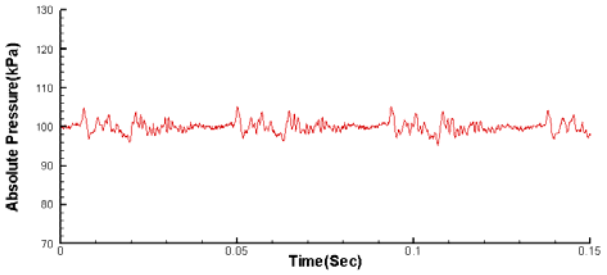
3.1.1 Pressure Data

Pressure data needed for numerical simulation were measured at the assigned points A, B and C for different engine speeds. Only the pressure data at point A is shown here because of space limitation. Figure 4 shows the pressure data measured at point A for an engine speed of 4000rpm, where rpm stands for revolution per minute. From Fig. 4 it is obvious that the pressure peak is proportional to the engine speed. The frequency of the pressure peak is 23Hz for 3000rpm, 31Hz for 4000rpm and 41Hz for 5000rpm, which agrees well with the theoretical values of 25Hz, 33Hz and 42Hz, respectively. The theoretical value of frequency (f) is obtained from the formula of f = rpm/(2 × 60s) for a four-stroke engine and f = rpm/(60s) for a two-stroke engine. The corresponding experimental period is 0.0436s for 3000rpm, 0.0325s for 4000rpm and 0.0246s for 5000rpm.

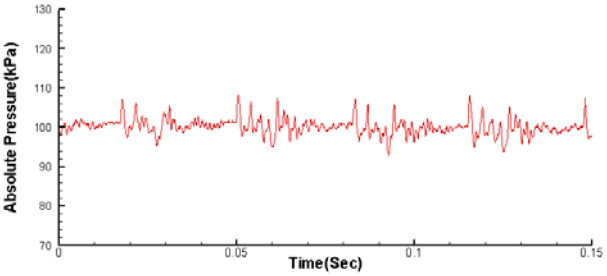
3.1.2 Temperature Data

The measured (average) temperatures at points A, B and C for 3000rpm were 473.07K, 473.59K and 473.97K respectively. The temperatures at these three points are increased to 564.14K, 566.80K and 568.42K for 4000rpm, and 576.92K, 578.80, 578.87K for

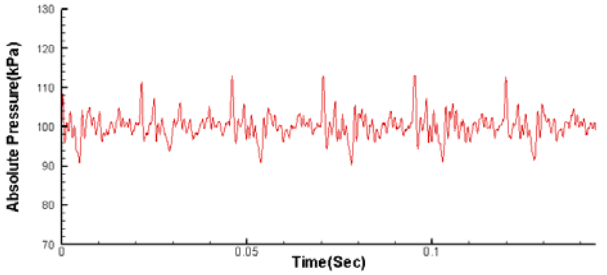
https://doi.org/10.1017/jmech.2011.62 Published online by Cambridge University Press



(a) 3000rpm



(b) 4000rpm



(c) 5000rpm

Fig. 4 Pressure fluctuations at point *A* for different engine speeds

5000rpm respectively. Note that point *A* is the closest to the pipe exit, point *B* is at the right of point *A* and point *C* is at the right of point *B*, as already indicated in Fig. 1. Obviously the measured (average) temperatures, which are not the instantaneously temperatures used for numerical simulation, may cause the discrepancy between the experimental and numerical *SPL* values.

3.1.3 Average Flow Velocity Data

The measured average flow velocity at point *C* was 25.29m/s for 3000rpm, 30.98m/s for 4000rpm and 37.94rpm for 5000rpm. Note that pint *C* is the tailpipe entrance of the simulation problem. Note that the average flow velocity, which is not the instantaneously flow velocity, used for numerical simulation, may cause the discrepancy between the experimental and numerical *SPL* values.

3.1.4 Sound Pressure Level Data

The spectrum of the measured sound pressure level at the distance of 0.25m and 0.5m from the pipe exit for various inclination angles and different engine speeds were collected. Only the result for the case of 0.5m and the inclination angle of 45° for the engine speeds of 3000rpm, 4000rpm and 5000rpm is shown in Fig. 5. Note that the measured sound pressure level has the unit of dB(*A*) which stands for the *A*-weighted sound pressure level. The *A*-weighting function can be found in reference 16. Thus the measured *SPL* value with dB(*A*) unit is different from that of numerical *SPL* value with dB unit defined by Eq. (6). It was found that the main frequency 330Hz for the case of 3000rpm, 330Hz for 4000rpm and 360Hz for 5000rpm.

3.2 Numerical Results

3.2.1 Propagation and Diffraction of Shock Wave

Numerical simulation is helpful for flow observation of blast wave propagation inside and outside the exhaust pipe. A blast wave has the feature of a shock wave front followed by expansion waves. Figure 6 shows the computational schlieren pictures of the blast wave propagation inside and outside the exhaust pipe for an engine speed of 4000rpm. Figure 6(a) shows a shock wave front (SF) has arrived near the pipe exit. After that, the shock wave diffracts around the pipe wall corner and expansion waves (EW) are generated in a circular fashion and propagate towards the pipe centerline and upstream, as shown in Fig. 6(b). At $t = 2.6$, the expansion wave front has passed the centerline. Later the expansion wave front arrives at the pipe wall, and will be reflected back as denoted by REW in Fig. 6(e). At $t = 3.6$, the reflected expansion waves passes the centerline again, as shown in Fig. 6(f). It is expected that the expansion wave front will be reflected back and forth inside the exhaust pipe while moving upstream.

For a larger time ($t = 30$), a vortex ring (V_1) with a slip line (SL) has been developed downstream of the pipe, as shown in Fig. 7(a). Moreover, the contact surface (CS) as seen in Fig. 6(a) has moved out of the pipe. Another shock wave (S_2) is moving from the left to the right. At $t = 40$, the second vortex ring (V_2) has been developed and acoustic waves (AW) have been generated. The second shock wave moves further to the right, as shown in Fig. 7(b). At $t = 45$ and 50, the second vortex ring (V_2) becomes larger, as seen from Figs. 7(c) and 7(d). At $t = 60$, the second shock wave moves to the pipe exit, as shown in Fig. 7(e), and is going to interact with the second vortex ring. At $t = 65$, the second shock wave is interacting with the second vortex ring, as shown in Fig. 7(f), causing a very complicated flow structure which is difficult for analysis.

Note that a vorticity vector ($\vec{\omega} = \nabla \times \vec{V}$) must satisfy the following vorticity transport equation for an inviscid flow:

$$\frac{D\vec{\omega}}{Dt} = -\vec{\omega}(\nabla \cdot \vec{V}) + (\vec{\omega} \cdot \nabla)\vec{V} - \frac{\nabla p \times \nabla \rho}{\rho^2} \tag{8}$$

Thus the vorticity generation in a three dimensional flow is attributed by three terms. The first term in the right-hand side of this equation involves in the flow compressibility, $\nabla \cdot \vec{V}$; the second term, $(\vec{\omega} \cdot \nabla)\vec{V}$, is

https://doi.org/10.1017/jmech.2011.62 Published online by Cambridge University Press

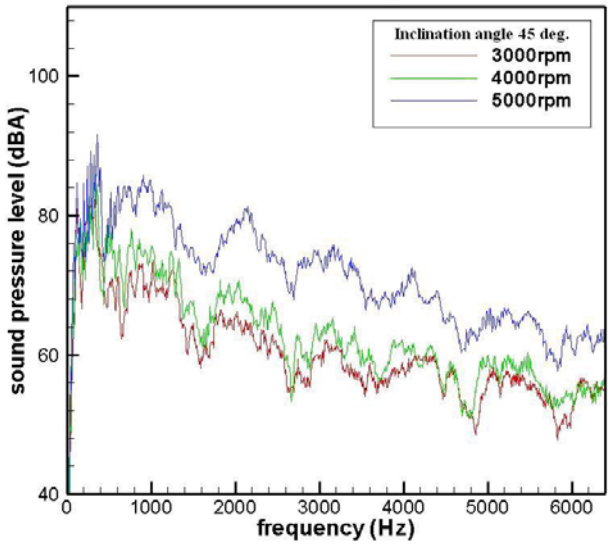


Fig. 5 Spectrum of the measured sound pressure level at 0.5m from the pipe exit for different engine speeds

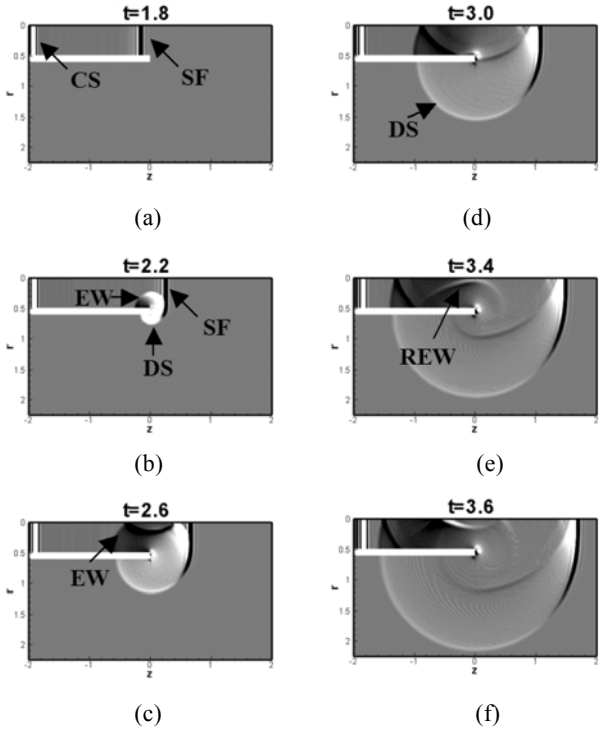


Fig. 6 Computational schlieren pictures at an early stage, 4000rpm. (CS denotes contact surface, SF for shock front, DS for diffracted shock, EW for expansion wave and REF for reflected expansion wave.)

not zero for an axi-symmetric case; and the third term is called the baroclinic effect due to the fact of the pressure gradient being not parallel to the density gradient. The baroclinic effect results from the diffraction of the shock wave around the pipe wall corner. The development of vortex rings partially contributes noise generation in the exhausted flow.

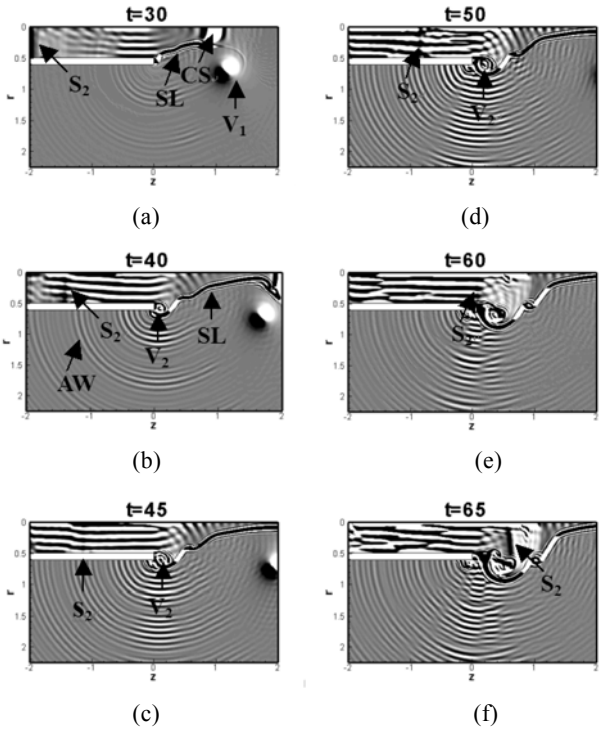


Fig. 7 Computational schlieren pictures at larger times, 4000rpm. (CS denotes contact surface, S_2 for the 2nd shock front, V_1 and V_2 for the 1st, 2nd vortex ring, SL for slip line, and AW for acoustic waves.)

3.2.2 Reflection of Expansion Waves Inside the Pipe

As seen from Figs. 5 and 6, expansion waves induced by shock wave diffraction will reflect back and forth inside pipe during propagating upstream. The expansion wave reflection results in the generation of radiated noise when the exhausted gas flows out of the pipe.

3.2.3 Interaction of Contact Surface with Vortex Ring

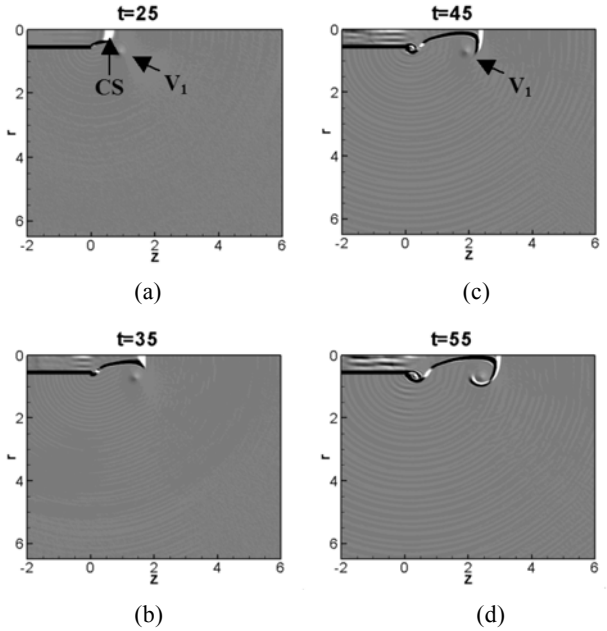
Figure 8 shows computational schlieren pictures for interactions of a contact surface with the induced vortex ring at different instants in the case of 4000rpm. As seen in Figs. 7(a) and 8(a), the contact surface has moved closer to the induced vortex ring. Later, at $t = 35 \sim 55$, the contact surface always interacts with the vortex ring, as shown in Figs. 8(b) and 8(c). In particular, at $t = 55$, the contact surface penetrates the vortex ring and moves with it downstream.

3.2.4 Sound Pressure Levels for Different Engine Speeds

A convergent solution can be obtained after iteration number of 43000, since the residual behaves in a periodic oscillation, as shown in Fig. 9(a). A cyclic residual of total energy is shown in Fig. 9(b). During this cycle indicated from point A to point G, there are 83 data points. The corresponding period is 0.0056s.

Figure 10 shows the sound pressure distributions at different instants that correspond to points A, B, C, F, during the iteration cycle as shown in Fig. 9(b) and the corresponding computational schlieren distributions. From Figs. 10(a1 ~ a4) it is clearly shown the radiated

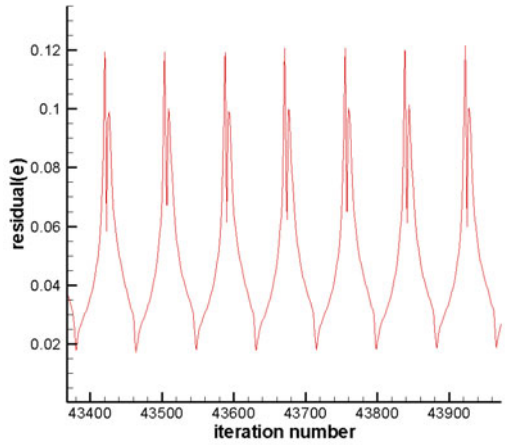
https://doi.org/10.1017/jmech.2011.62 Published online by Cambridge University Press



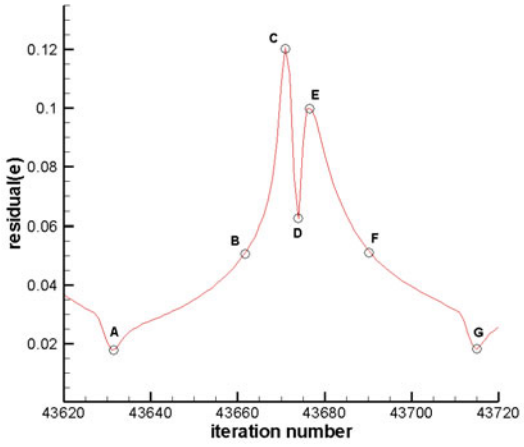
(a) (c)

(b) (d)

Fig. 8 Computational schlieren pictures for interactions of a contact surface with a vortex ring at different instants, 4000rpm

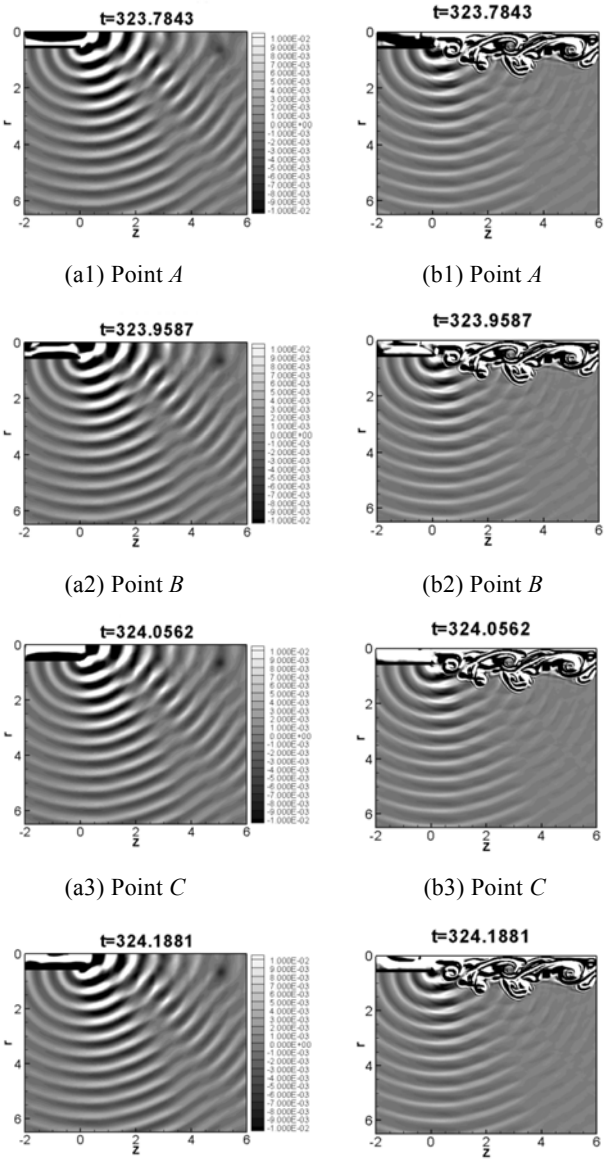


(a)



(b)

Fig. 9 (a) a convergent residual history and (b) an enlarged cycle, 4000rpm



(a1) Point *A* (b1) Point *A*

(a2) Point *B* (b2) Point *B*

(a3) Point *C* (b3) Point *C*

(a4) Point *F* (b4) Point *F*

Fig. 10 (a1 – a4) the sound pressure distributions and (b1 – b4) the computational schlieren distributions at different instants, corresponding to points *A*, *B*, *C*, *F* in Fig. 9(b), respectively, 4000rpm

sound waves with directivity. From Figs. 10(b1 ~ b4) we clearly see the radiated sound waves and the cortex rings shed downstream. Note that the inviscid-flow vortices predicted is stronger than those for a viscous flow, resulting in higher noise prediction.

Figure 11 shows the *SPL* distributions corresponding to Fig. 10. The *SPL* distributions clearly indicate the sound lobes which have their inclination angles. There are three sound lobes: One major sound lobe and two minor ones.

We use the computational near-field SPL_1 at $z = 5.43$ ($r_1 = 12.5$cm) for predicting the far-field SPL_2 at $r_2 = 50$cm where we have the experimental data of *SPL* for reference by the following equation.

$$SPL_2 = SPL_1 - 20\log(r_2 / r_1) \tag{9}$$

https://doi.org/10.1017/jmech.2011.62 Published online by Cambridge University Press

The predicted and experimental results of *SPL* values are tabulated in Table 1 and plotted in Fig. 12 for reader's reference. The predicted *SPL* cannot be compared with the experimental *SPL* because of several reasons. These reasons are (1) the inlet flow boundary condition used for numerical simulation is different from the real one in experiment; (2) the outflow boundary condition used does not take the suctioned-out flow in the anechoic room into account; (3) the predicted and experimental *SPLs* are in different units; (4) the inviscid flow is assumed, resulting in a stronger vortex ring predicted than that of a viscous flow; and (5) a simplified formula, Eq. (8) is used for prediction. The predicted *SPL* at the inclination angle of 30° ~ 90° is between 120dB to 135dB. The measured *SPLs* are between 101-110.4 dB(A). If one makes an unfair comparison, the relative error can range from 17% to 31% for 3000rpm, 12% ~ 25% for 4000rpm, and 5% ~ 23% for 5000rpm.

Table 1 Predicted and experimental *SPLs* at 0.5m from the pipe exit for different engine speeds (rpm)

Inclination Angle (deg.)	Engine Speed					
	3000rpm		4000rpm		5000rpm	
	Predicted (dB)	Exp. (dBA)	Predicted (dB)	Exp. (dBA)	Predicted (dB)	Exp. (dBA)
15	118.77	101.2	124.44	106.3	104.86	110.4
30	129.88	101.2	126.53	106.1	125.41	110.0
45	125.42	101.0	119.85	106.3	126.01	109.1
60	132.79	101.0	130.69	106.2	134.65	109.0
75	132.39	101.0	132.84	105.9	126.38	109.1
90	129.59	101.0	129.92	105.8	125.95	109.0

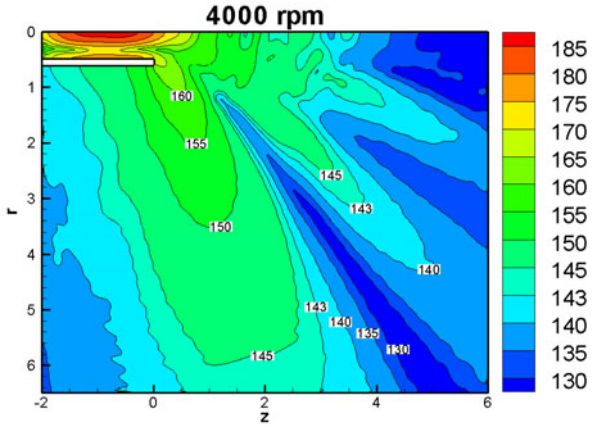


Fig. 11 The sound pressure distribution, 4000rpm

4. CONCLUSIONS

In this study, both experimental and numerical methods were employed for investigating the near-field acoustics and flow structure of a motorcycle's exhaust pipe. In numerical simulation, the high-resolution method of a 5th-order WENO scheme and a 4th-order Runge-Kutta scheme was used for solving Euler equations for a pulsating flow in cooperation of parallel computation on 4 personal computers with dual processors. In experiment, measurements of the pressure, temperature, and average flow velocity at the pipe inlet were conducted to meet the need of the 5th-order accuracy scheme in numerical simulation.

It is found that the back-and-forth reflection inside the pipe due to the shock wave diffraction around the pipe end is the mechanism of radiating sound waves from the exhaust pipe exit. The vortex rings induced by the shock wave passing through the exhaust pipe may contribute the *SPL* more than that in real flow because a higher strength of vortex ring is predicted in inviscid-flow simulation. Moreover, the sound waves radiated from the pipe exit is successfully simulated and analyzed. There are three sound lobes are found for the engine speed of 4000rpm, which possess their directivity. This study establishes a stepping stone for studying a complicated motorcycle's exhaust pipe flow and finding other further noise reduction methods such as porous pipe wall of a tailpipe in addition to the existing mufflers. It is suggested that a larger computational domain than the present one used is better for sound pressure level prediction for future study by increasing the number of CPUs.

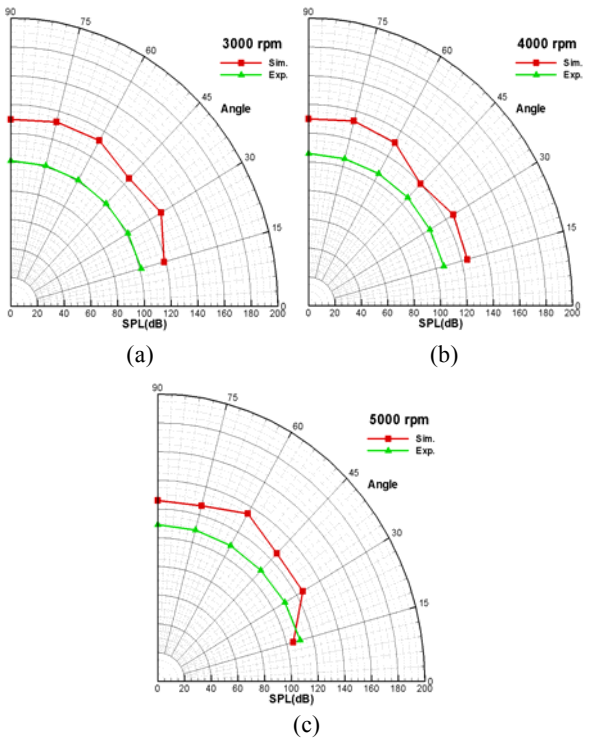


Fig. 12 Comparison of experimental and computational *SPLs* at $r = 0.5$m

https://doi.org/10.1017/jmech.2011.62 Published online by Cambridge University Press

ACKNOWLEDGEMENT

This support for this study under the grant, NSC 96-2221-E-269-013-MY3, of the National Science Council was appreciated.

REFERENCES

1. "Standard of Noise Control for Automotive Vehicles," Environmental Protection Administration, Taiwan, (2008).
2. Lighthill, M. J., "On Sound Generated Aerodynamically. I. General Theory," *Proceedings of the Royal Society of London. Series A*, **211**, pp. 564–587 (1952).
3. Kim, H. D. and Setoguchi, T., "Study of the Discharge of Weak Shocks from an Open End of a Duct," *Journal of Sound and Vibration*, **226**, pp. 1011–1028 (1999).
4. Higashima, J. and Iwamoto, J., "Experimental Study of Exhaust Noise Generated by Pulsating Flow downstream of Pipe End," *JSAE Review*, **20**, pp. 73–79 (1999).
5. Endo, M., Futagami, Y. and Iwamoto, J., "Relation Between the Flow Pattern Downstream of Duct and the Noise," *JSAE Review*, **21**, pp. 125–132 (2000).
6. Chen, H. and Liang, S. M., "Planar Blast/Vortex Interaction and Sound Generation," *AIAA Journal*, **40**, pp. 2298–2304 (2002).
7. Inoue, O. and Hattori, Y., "Sound Generation by Shock-Vortex Interactions," *Journal of Fluid Mechanics,* **380**, pp. 81–116 (1999).
8. Liang, S. M. and Lo, C. P., "Shock/Vortex Interactions Induced by Blast Waves," *AIAA Journal*, **41**, pp. 1341–1346 (2003).
9. Liang, S. M., Chung, W. T. and Chen, H., "Numerical Investigation of Reflected Shock/Vortex Interaction near an Open-ended Duct," *AIAA Journal*, **43**, pp. 349–356 (2005).
10. Kim, H.-D., Kweon, Y.-H. and Setoguchi, T., "A Study of the Weak Shock Wave Propagating through an Engine Exhaust Silencer System," *Journal of Sound and Vibration*, **275**, pp. 893–915 (2004).
11. Gabard G. and Astley, R. J., "Theoretical Model for Sound Radiation from Annular Jet Pipes: Far- and Near-field Solutions," *Journal of Fluid Mechanics,* **549**, pp. 315–341 (2006).
12. Gabard, G., "Near- to Far-field Characteristics of Acoustic Radiation Through Plug Flow Jets," *Acoustical Society of America*, **1124**, pp. 2755–2766 (2008)
13. Demir, A. and Rienstra, S. W., "Sound Radiation from an Annular Duct with Jet Flow and a Lined Centerbody," 12th AIAA/CEAS Aeroacoustics Conference, 8-10 May, 2006, Cambridge, MA. USA, AIAA Paper 2006-2718.
14. Jiang, G.-S. and Shu, C.-W., "Efficient Implementation of Weighted ENO Schemes," *Journal of Computational Physics*, **126**, pp. 202–228 (1996).
15. Thompson, W., "Time Dependent Boundary Conditions for Hyperbolic Systems," *Journal of Computational Physics*, **68**, pp. 1–24 (1987).
16. Chung, W. T., "Analysis of the Flow Field and Noise Generation Mechanism inside and near the Exit of a Vehicle's Exhaust Pipe," *Department of Aeronautics and Astronautics*, National Cheng Kung University, p. 80 (2007).

(Manuscript received September 14, 2010, accepted for publication June 7, 2011.)

https://doi.org/10.1017/jmech.2011.62 Published online by Cambridge University Press